High-Resolution Mapping of Electron-Beam-Excited Plasmon Modes in Lithographically Defined Gold Nanostructures

Ai Leen Koh,[†,ǁ] Antonio I. Fernández-Domínguez,[‡] David W. McComb,*[,†] Stefan A. Maier,*[,‡] and Joel K. W. Yang*[,§]
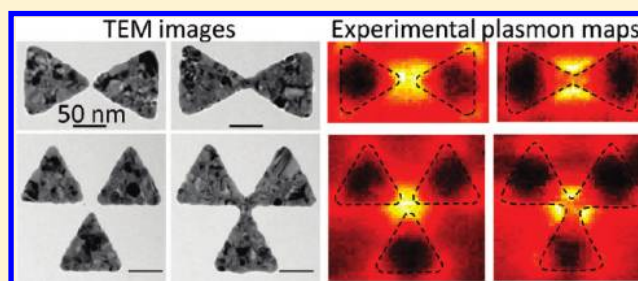
[†]Department of Materials and [‡]Department of Physics, Imperial College London, London SW7 2AZ, United Kingdom
[§]Institute of Materials Research and Engineering, A*STAR, Singapore 117602

S *Supporting Information*

ABSTRACT: We demonstrate the use of high-resolution electron beam lithography to fabricate complex nanocavities with nanometric spatial and positional control. The plasmon modes of these nanostructures are then mapped using electron energy-loss spectroscopy in a scanning transmission electron microsope. This powerful combination of patterning and plasmon mapping provides direct experimental verification to theoretical predictions of plasmon hybridization theory in complex metal nanostructures and allows the determination of the full mode spectrum of such cavities.

KEYWORDS: Electron energy-loss spectroscopy, localized surface plasmons, electron-beam lithography

Plasmon resonances in nanostructures allow the concentration of light into subdiffraction limited volumes and high electric-field intensities,[1,2] with numerous demonstrations of scientific and technological importance.[3−9] While advances in numerical simulation capabilities continue to contribute to the rapid progress in this field, direct experimental visualization of the plasmon modes in the nanoscale vicinity of designer plasmonic nanostructures is currently lacking. In this article we demonstrate a method that is suited for such design-verification purposes, crucially allowing for a determination of the full mode spectrum of plasmonic nanostructures, including dark modes.[10,11] Dark modes are plasmonic resonances that couple only weakly to free-space radiation and whose main decay channel is via absorption within the particle, rather than radiative damping. Probably the simplest example of dark plasmonic modes is the high-order multipolar Mie resonances in small spherical nanoparticles, in which retardation effects are not strong enough to prevent their probing by optical methods.[12] Of particular importance is a knowledge about the spectral location of dark modes of the system, as these modes can lead to efficient quenching of nearby emitters.[13] Moreover, as we show below, these dark modes can lie spectrally very close to bright modes used for emission enhancement, even in the widely used bow tie nanoantenna geometry. Hence, among other structures of interest, we map for the first time the full plasmon modes of these nanoantennas.

As the electromagnetic field distribution of plasmon resonances is confined to the near field of the metal nanostructures, imaging their plasmon modes is challenging as it requires an interaction with this near field with sufficient spatial resolution. Imaging of plasmons can be achieved optically using a scanning near-field optical microscope (SNOM) but is limited in resolution by the aperture of the scanning tip to ∼50 nm,[14] which is already at the length scale of plasmonic resonators. On the other hand, with highly energetic electrons one can simultaneously excite the plasmon modes and register with nanometer resolution the positional information of the excitation. The excitation of plasmon modes can be observed by detecting emitted optical radiation or by measuring the energy loss of the electron.[15,16] The former, known as cathodoluminescence (CL),[17,18] has been used to resolve higher-order plasmons and in small metallic nanostructures.[12,19] However, CL can only efficiently access bright modes and is limited by signal intensity and beam quality, although the spatial resolution of this technique has recently been reported to go below 2 nm.[20] On the other hand, electron energy-loss spectroscopy (EELS) enables the probing of the local density of states for plasmonic nanoparticles, which fully characterizes their optical properties.[21,22] Furthermore, EELS captures information about dark modes in addition to bright modes and, hence, unravels the full modal spectrum of a plasmonic nanocavity. For plasmonic nanocavities to find use as active device elements, for example, interacting with localized (quantum) emitters, it is crucial to establish a fabrication/characterization methodology that allows for the mapping of its full mode spectrum.

This article demonstrates an approach to address the challenges of mapping plasmon modes on strategically designed nanostructures. We patterned metallic (gold) nanostructures directly onto silicon nitride (SiN) membranes using high-resolution
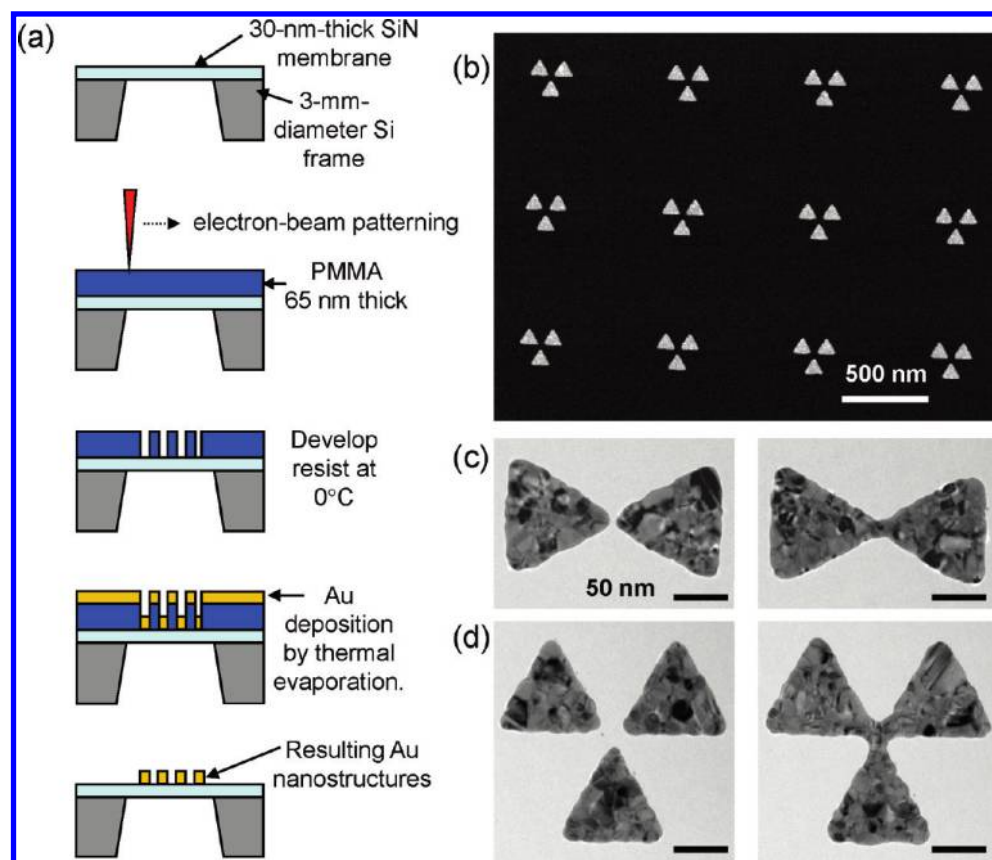
Figure 1. (a) Process flow for top-down patterning of metal nanostructures on a SiN membrane for plasmon mapping with EELS. (b) Low-magnification annular dark-field STEM image of an array of nanostructures with well-defined dimensions and orientations. Each nanostructure comprises three disconnected triangles. (c, d) Bright-field TEM images of the triangle systems reported in this paper: two disconnected triangles (c, left); two connected triangles (c, right); three disconnected triangles (d, left); three connected triangles (d, right). The scale bar in each of the figures denotes 50 nm.

electron-beam lithography,[23,24] thus gaining flexibility and control in structure design, size, and spatial arrangement. The plasmon resonances and maps can then be obtained on various configurations of nanostructures on this sample using a (scanning) transmission electron microscope ((S)TEM) equipped with a monochromator and an electron energy-loss spectrometer. In contrast to previous works based on EELS mapping of chemically synthesized metal nanoparticles,[25−30] lithographically defining the nanostructures allows us to systematically study plasmon modes in closely spaced nanostructures with various well-defined configurations and orientations. In the following, we choose the popular triangular motif as the basic unit of more complex dimer (bow-tie antenna) and trimer nanoantennas, and demonstrate mapping of their modal spectra. These modes are interpreted in terms of hybridizations between the fundamental dipolar and quadrupolar modes of the individual triangles. We further present a straightforward semiquantitative modeling approach that shows excellent agreement with our experimental results.

Although EELS mapping of plasmon modes in individual nanoprisms have been previously reported in individual nanoprisms and other nanostructures,[26,31] to the best of our knowledge, there has been no report to date about the full electromagnetic behavior examined at high spatial resolution and including nonradiating modes, when these nanoprisms are brought to close proximity. We patterned structures consisting of groups of two or

three triangles with ∼100 nm sides and ∼15 nm thickness, and systematically varied the distance between the triangles until they were connected. The samples were fabricated on 30 nm thick SiN membranes using a process described previously[32] and summarized in Figure 1a (section 1, Supporting Information). Panels c and d of Figure 1 show TEM bright-field images of triangle nanostructures with varying intertriangle spacing and configurations. The polycrystallinity of the Au nanostructures is manifested by the varying diffraction contrast from different crystal grains giving the appearance of bright and dark domains within the triangles.

EELS experiments were performed using an FEI Titan (S)TEM operated at 300 kV (section 3, Supporting Information). It is equipped with a spherical-aberration image corrector, a monochromator, and a Gatan Tridiem 866 EEL spectrometer with 2048 spectral-readout channels. The spatial and energy resolutions of the microscope in monochromated STEM mode are 0.3 nm and 0.2 eV (defined as the full width at half-maximum of the zero-loss peak (ZLP)), respectively. Figure 1b shows an annular dark field (ADF)-STEM image of an array of gold nanotriangles arranged in groups of three as an example of the level of positional and shape control achievable by the process described above.

To study the nature of the excitation modes, full electrodynamics simulations were performed using COMSOL Multiphysics (section 2, Supporting Information). The experimental nanoparticles were modeled using simple geometries (neglecting
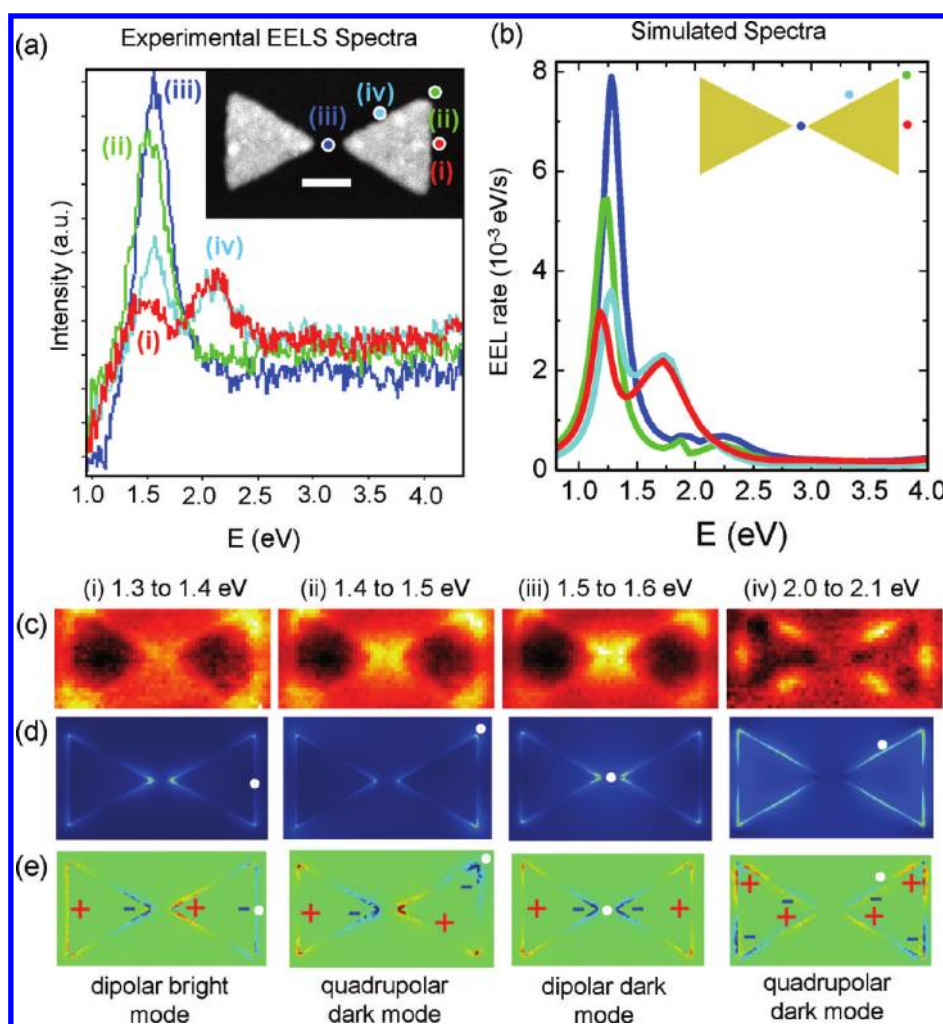
Figure 2. (a) Extracted experimental EEL spectra of a bow-tie antenna from the (i) outer edge, (ii) corner, (iii) junction, and (iv) inner edge of the structure. The ADF-STEM image of the dimer is inset. The points where the EEL spectra are extracted are denoted with the same color representations. The scale bar denotes 50 nm. (b) Simulated spectra of the bow-tie antenna at the same corresponding points as in (a) showing excellent agreement between experimental and simulated results. (c) Plasmon maps obtained experimentally from integrated EELS signal intensity over the energy range of (i) 1.3−1.4 eV, (ii) 1.4−1.5 eV, (iii) 1.5−1.6 eV, and (iv) 2.0−2.1 eV. (d) Simulated electric-field intensity |E| maps. (e) Simulated charge-density maps. The excitation positions of the electron beam that resulted in the maps in (d) and (e) are indicated by the white dot. The roman numerals (i−iv) indicate the peak positions to which these excitations correspond to as labeled in (a).

fabrication asymmetries and imperfections), and the structure dimensions considered in the calculations were extracted from annular dark-field STEM images of the samples. The use of COMSOL was advantageous in our simulations as it enabled a highly nonuniform discretization mesh to be used for accurate treatment of the different length scales involved in the solution of Maxwell's equations for the samples under study: the vacuum wavelength of the plasmon modes (hundreds of nanometers), nanoparticle size (tens of nanometers), and metal skin depth (several nanometers). The use of adaptive meshes in our calculations also enabled us to model the experimental nanoparticles by simple but sharp triangular geometries, with chamfer radii below 1 nm. In the case of composite touching nanoparticles, triangles were overlapped to model the experimental structure. In all the simulations, linear electric currents of ∼50 pA (following experimental conditions) oriented normally to the substrate plane were employed as the excitation source.

Results of several examples of fabricated nanocavities and their corresponding plasmon maps will be presented next. Collectively,

these examples demonstrate the unique capabilities of EELS for the spectral and spatial mapping of the full mode spectrum of these plasmonic nanocavities.

Figure 2 shows the results obtained from a bow-tie antenna (disconnected dimer) configuration with a gap size of ∼25 nm. Different modes are excited by positioning the electron-beam at different positions relative to the nanostructure. For instance, the EEL spectra corresponding to excitations at the outer edge (i), corner (ii) gap (iii), and inner edge (iv) of the triangles are presented in Figure 2a, with the corresponding ADF-STEM image inset. Simulated spectra with the electron beam directed at the corresponding positions are shown in Figure 2b. The relative amplitudes and positions on the energy axis of resonances from the simulation results closely match those from the experimental results. No fitting parameters were used in the simulations. Each peak in the spectra corresponds to modes supported by the bow-tie antenna as a result of the coupling/hybridization of the simpler plasmon modes in isolated nanoparticles.[26] This coupling is evidenced by the resonance peak from the gap excitation
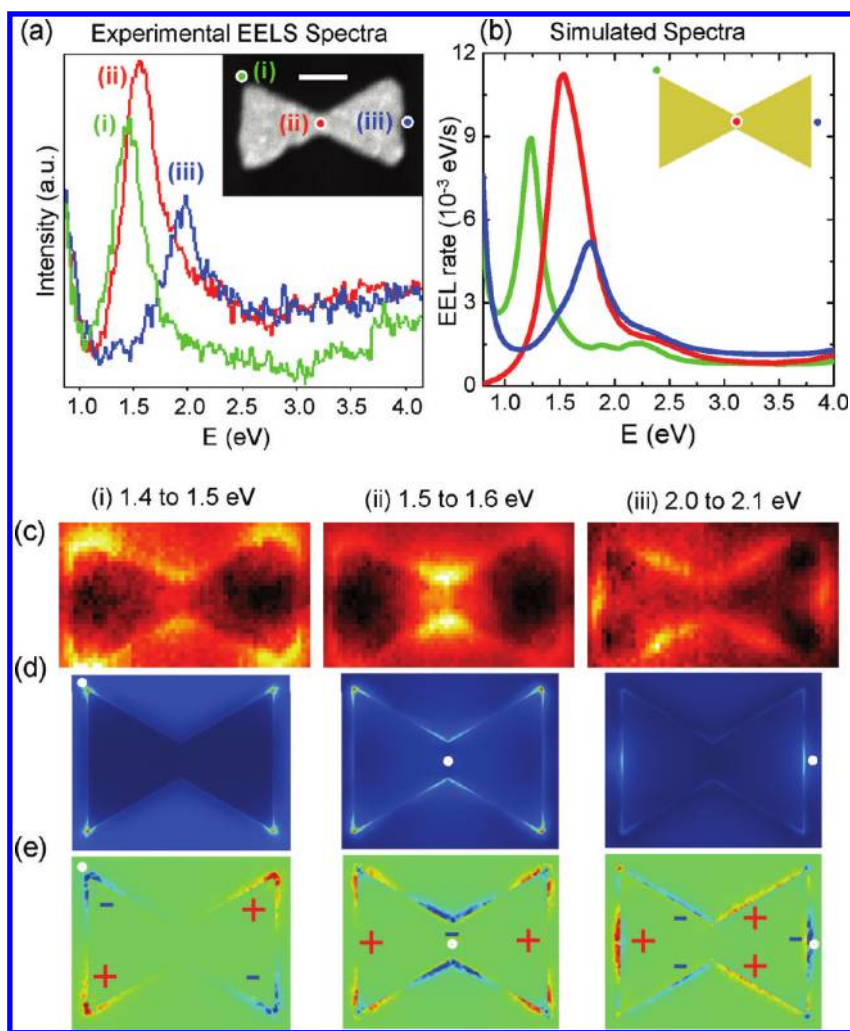
Figure 3. (a) Extracted experimental EEL spectra of a connected dimer from the corner (i), junction (ii), and edge (iii). The ADF-STEM image of the dimer is inset. The scale bar denotes 50 nm. (b) Simulated spectra of the connected dimer at the corresponding excitation points as in (a). (c) Plasmon maps obtained experimentally from integrated EELS signal intensity over the energy range of (i) 1.4−1.5 eV, (ii) 1.5−1.6 eV, and (iii) 2.0−2.1 eV. (d) Simulated electric-field intensity |E| maps. (e) Simulated charge-density maps. The excitation positions of the electron beam that resulted in these maps are indicated by the white dot. The roman numerals (i−iii) indicate the resonance peak positions to which these excitations correspond to as labeled in (a).

at 1.6 eV that is blue-shifted by ∼0.1 eV relative to that from the corner excitation. As explained below, this blue-shifted peak corresponds to a dark mode and is spectrally close to the bright mode at 1.5 eV. When the spectrum image was extracted in energy slices with 0.1 eV intervals, we obtained plasmon excitation maps as shown in Figure 2c. (See section 4 in the Supporting Information for a full range of these dynamic maps.) While these maps do not directly correspond to the photonic density of states,[22] they are very much related to the spatial field distribution of the plasmon modes supported by the nanostructure. The blue-shifted mode had a distinct plasmon map (Figure 2c(iii)) when compared to the corner (Figure 2c(ii)) and edge (Figure 2c(i,iv)) modes. As can be seen in the plasmon map in Figure 2c(iii) the optical energy in this dark mode was predominantly confined in the gap region.

Upon inspection, we observe that the peaks from different excitation points within the 1.3−1.7 eV energy window in Figure 2a are slightly shifted from each other. These shifts are a result of plasmon hybridization[33] and can be understood by observing the simulation plots of the charge-density maps shown

in Figure 2e(i−iii). These are plots of the instantaneous charge densities that provide phase information of the plasmon-resonant fields. The excitation at the outer side produces a dipolar bright mode as shown in Figure 2e(i). This mode is also the one that is excited by far-field optical illumination with the electric field polarization along the length of the bow-tie antenna. The electrostatic attraction between the triangles in this dipolar bright mode results in this being the lowest-energy peak. The mode generated by excitation at the corner leads to a quadrupolar-like charge distribution as shown in Figure 2e(ii). We can understand this charge distribution as the electron beam inducing a dipole in the right triangle tilted 60° with respect to the dimer axis that in turn induces a horizontal dipole on the left triangle. Finally, the peaks obtained from the excitations at both the junction and inner edge give rise to the same dipolar dark mode with a charge-density map as shown in Figure 2e(iii). This dipolar dark mode has the highest energy peak in the 1.3−1.7 eV energy range, due to electrostatic repulsion of like charges at the gap region.

Electrons directed at the corner and junction efficiently excited only the low-energy modes centered about 1.5 eV.
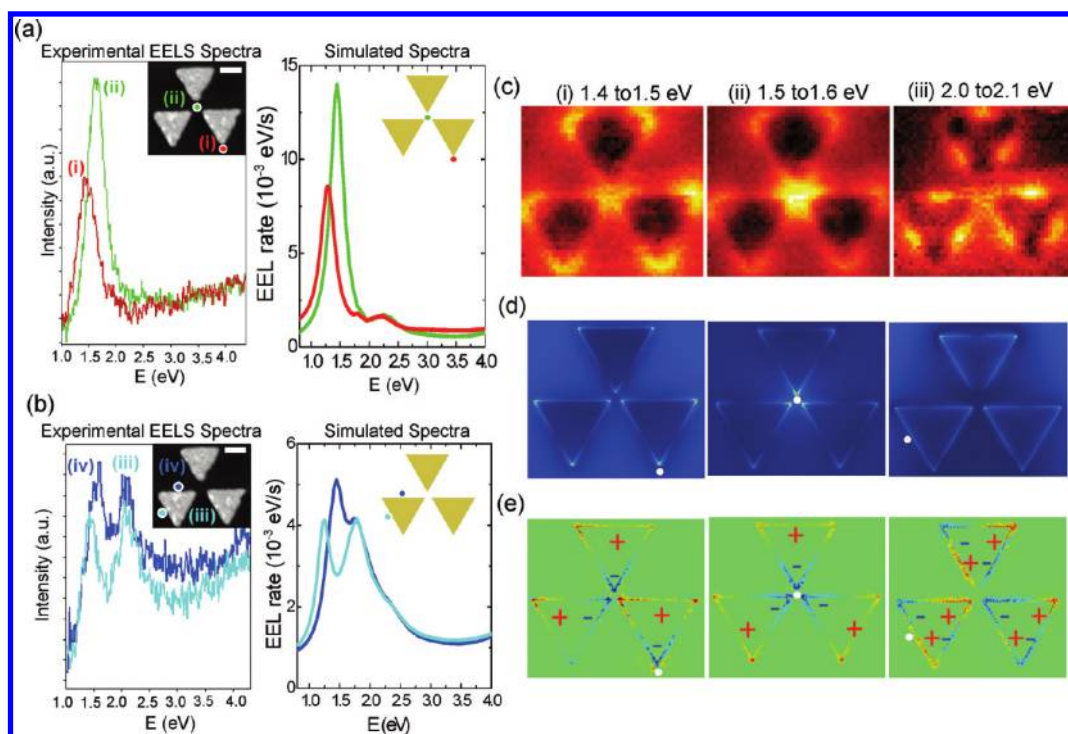
Figure 4. (a) Experimental and simulated EEL spectra for the disconnected trimer configuration for excitations at the (i) junction and (ii) corner. (b) Experimental and simulated EEL spectra for excitations at the (iii) outer edge and (iv) inner edge. The ADF-STEM image of the nanostructure is shown in the insets of the experimental EEL spectra and labeled with the corresponding excitation positions. The scale bar denotes 50 nm. (c) Plasmon maps showing the integrated EEL signal intensity maps over the energy ranges of (i) 1.4−1.5 eV, (ii) 1.6−1.7 eV, and (iii) 2.0−2.1 eV. (d) Simulated electric-field intensity $|E|$ maps. (e) Simulated charge-density maps. The excitation positions of the electron beam that resulted in the maps in (d) and (e) are indicated by the white dot. The roman numerals (i−iii) indicate the peak positions to which these excitations correspond to as labeled in (a).

However, those directed at the edges excite high-energy (2 eV) modes as well. These high-energy modes have a quadrupolar dark character and arise from the coupling of the quadrupolar modes supported by isolated triangles, as shown in Figure 2e(iv). The simulated electric-field intensity $|E|$ maps are shown in Figure 2d for the given excitation points as indicated in the figures. Note that these theoretical maps show the electric-field distributions for a given excitation point, unlike the EELS maps, which were obtained by integrating the EELS signal within a 0.1 eV energy window for excitation points across the entire region of interest. Therefore, only at energies for which the response of the structure is governed by a single plasmonic mode, such as the dark mode that peaks at 1.6 eV, can theoretical and experimental maps be compared. At energies for which a number of degenerate plasmon modes are sustained, e.g., the quadrupolar dark modes in the 2.0−2.1 eV range, the experimental plasmon map correspond to the superposition of all of them, whereas only one is shown in the calculations.

By systematically reducing the size of the gap between the triangles patterned using electron-beam lithography, we obtained triangles that were eventually connected as shown in the inset of Figure 3a. In this connected dimer, electrons are free to flow from one triangle to the other, leading to charge-transfer plasmons.[27,28] Here, charge neutrality in a single triangle need not be maintained, unlike the case for the bow-tie antenna. The EELS and simulation results of the connected dimer are shown in Figure 3. The simulation and experimental results are again in good agreement with each other. The plasmon maps in Figure 3c display modes that seem to be in close correspondence to those of the bow-tie antenna. Three different excitations—corner,

junction, and edge—are considered in this case. However, simulation results show that charge-density distributions are entirely different as soon as the triangles are connected. The major difference arises from the excitations at the outer edges; cf. Figure 2a(i) and Figure 3a(iii). Note the presence of two peaks in the spectra of Figure 2a(i), while only one is present in that of Figure 3a(iii); i.e., the low-energy peak at ∼1.5 eV is missing in the case of the connected triangles. The reason for this difference is that charge neutrality dictates that the lowest-energy mode for the bow-tie antenna needs to consist of two aligned dipoles as shown in Figure 2d(i). However, with charges free to move from one triangle to the other in the connected dimer, the lowest energy mode is a single dipole that spans the entire length of the structure, with a net positive charge in one triangle and a net negative charge in the other. Thus, the dipolar bright mode at 1.5 eV is replaced by much lower energy (<1 eV) dipolar bright mode, which is also consistent with the "large renormalization" as reported by Tolga Atay et al.[34] The charge-density map and the corresponding resonance peak (<1 eV) for this mode are observed in the simulations. However, this peak was not observed experimentally as it was concealed within the zero-loss peak of the EEL spectrum.

The EELS data for the case of three disconnected triangles with a gap of ∼23 nm are presented in Figure 4. Three distinct modes excited by positioning the electron beam at the corner, gap, and edge of the structures are shown in the plasmon maps in Figure 4c. Similar to the case of bow-tie antennas, the excitations at the corners (Figure 4a) produce a single resonance peak, while excitations at the edges (Figure 4b) produce two resonant modes. However, in this trimer configuration, we observe a
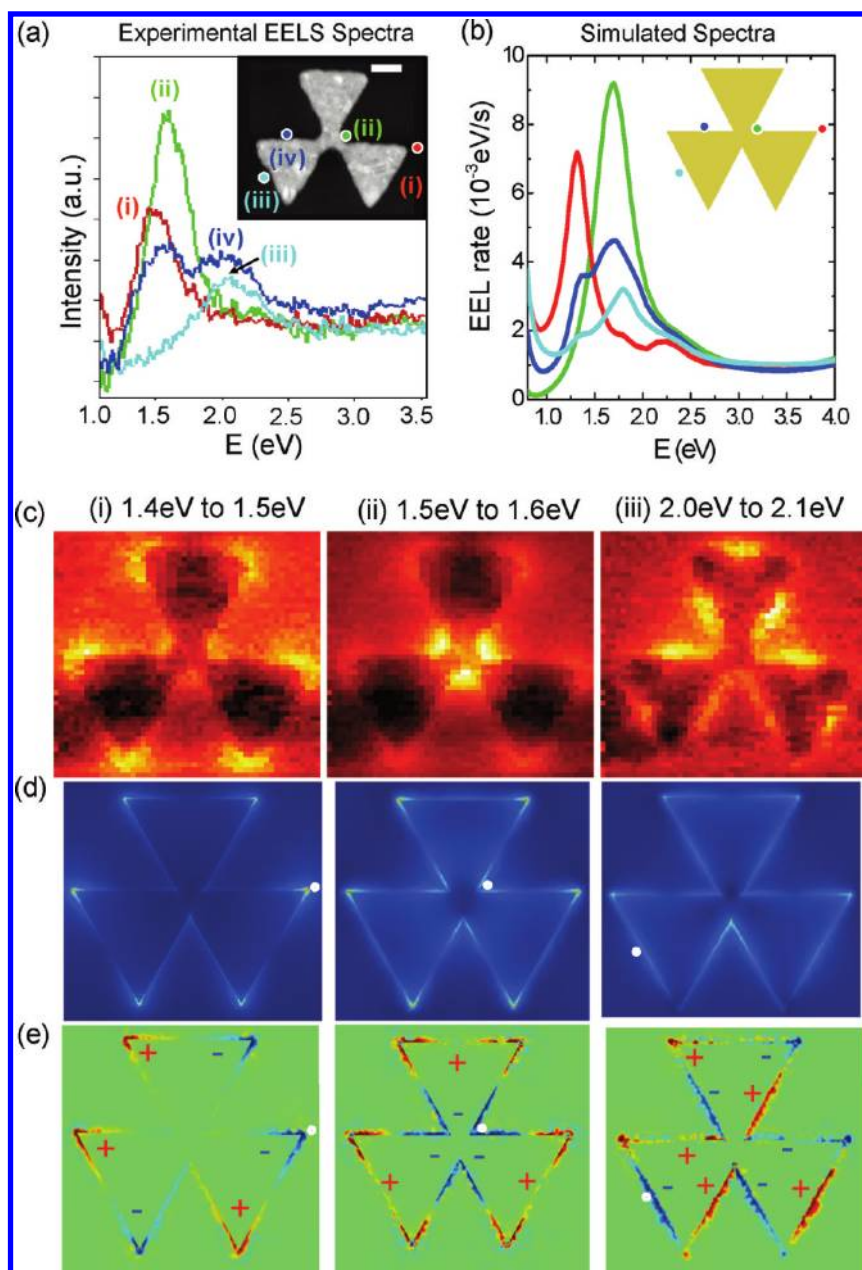
Figure 5. (a) Extracted experimental EEL spectra of a connected trimer from the (i) corner, (ii) junction, (iii) outer edge, and (iv) inner edge. The ADF-STEM image of the trimer is shown inset. The scale bar denotes 50 nm. The points where the EELS data were extracted are in the same color representation. (b) Simulated spectra of the disconnected trimer at the same corresponding points as in (a). (c) Plasmon maps showing the integrated EEL signal intensity maps over the energy ranges (i) 1.4−1.5 eV, (ii) 1.5−1.6 eV, and (iii) 2.0−2.1 eV. (d) Simulated electric-field intensity |E| maps. (e) Simulated charge-density maps. The excitation positions of the electron beam that resulted in the maps in (d) and (e) are indicated by the white dot. The roman numerals (i−iii) indicate the peak positions to which these excitations correspond to as labeled in (a).

larger blue shift of ∼0.2 eV between the junction and corner resonances (cf. Figure 4a(i) and (ii)) compared to the corresponding blue shift of ∼0.1 eV for the bow-tie antenna. This larger blue shift is attributed to the electrostatic repulsion that is stronger in the trimer configuration than it is in the bow-tie configuration, due to the presence of an additional corner. The relative energy positions of the resonance peaks can, again, be understood in terms of the charge attraction/repulsion as shown in the charge density maps in Figure 4e. For instance, Figure 4e(i) shows that corner excitations induce a dipole in the closest triangle that in turn induces *attracting* dipoles in the neighboring

triangles. On the other hand, the excitation at the gap induces *repelling* like charges among the closest corners of the three triangles seen in Figure 4e(ii). The excitation at the gap also produces a larger resonance peak than those at the other corners, due to more efficient transfer of energy from the incident electron to the plasmon mode. Similar to the case of dimers, this increased EEL rate is due to the strong (out-of-plane) electric fields of the dark plasmonic mode, as demonstrated in Figure 4d(ii).

Finally, the case of three touching triangles is displayed in Figure 5. Similar features as in the disconnected trimer configuration are observed. For instance, a single plasmon mode is

excited with the electron beam position at the corners (Figure 5a(i)) with the resonant mode at the junction blue shifted relative to the other corners (Figure 5a(ii)). With the three triangles connected, electrons are again free to flow from one triangle to the others. Hence, similar to the case of the connected dimer in Figure 3, excitations at the outer edges produce only a single observable resonant mode as in Figure 5a(iii). A low-energy plasmonic mode exists but is concealed by the ZLP of the EEL spectrum. On the other hand, excitation at the inner edge (Figure 5a(iv)) gives rise to two spectral peaks unlike the peak excited by the outer edge. This difference is related to the proximity of the inner edge excitation to two triangular particles, which leads to the appearance of modes with more complex symmetries in the same energy range as in the junction excitation. The plasmon maps for the three distinct modes are shown in Figure 5c for the energy slices indicated. The corresponding electric-field intensity maps and charge-density distributions are shown in panels d and e of Figure 5, respectively.

In conclusion, plasmonic modes from structures defined by high-resolution electron-beam lithography were mapped using electron-beam excitations in a transmission electron microscope equipped with EELS. The metal nanostructures exhibited plasmon resonances that were similar to those of chemically synthesized metal nanoparticles despite their polycrystallinity. Due to the ability to control the relative orientation and separations between structures defined lithographically, we showed that differences in nanoparticle configurations, e.g., nontouching versus touching triangles and dimers versus trimers, exhibited a rich variety of plasmonic responses. In particular, we observed that bow-tie antennas had dark and bright modes that are spectrally close, which could explain the asymmetric emission spectra of molecules whose fluorescence was enhanced when placed in the junction region of these bow-tie antennas. To gain understanding of the variety of plasmon modes observed, we modeled our experimental setup in COMSOL obtaining an excellent agreement between theory and experiment without fitting parameters. This combination of high-resolution electron-beam patterning and EELS mapping techniques enables one to scrutinize plasmon resonances for a range of nanostructures and could have potential for use in systematic verification of designer plasmonic nanostructures. In addition, due to the high-resolution nature of the lithography and measurement techniques described, we anticipate that this capability could be used to investigate plasmonic effects in nanometer dimensions, where quantum-mechanical effects become relevant.[35]

ASSOCIATED CONTENT

ⓈSupporting Information. Information on (1) sample fabrication, (2) theoretical modeling and simulations, (3) dimensions of nanoparticles, and (4) integrated EEL signal intensity maps. This material is available free of charge via the Internet at http://pubs.acs.org.

AUTHOR INFORMATION

Corresponding Author
*E-mail: (D.W.M) d.mccomb@imperial.ac.uk; (S.A.M) s.maier@imperial.ac.uk; (J.K.W.Y) yangkwj@imre.a-star.edu.sg.

Present Addresses
∥Currently at the Stanford Nanocharacterization Laboratory, Stanford University, Stanford, CA 94305, United States.

REFERENCES

(1) Barnes, W. L.; Dereux, A.; Ebbesen, T. W. *Nature* **2003**, *424* (6950), 824–30.

(2) Schuller, J. A.; Barnard, E. S.; Cai, W.; Jun, Y. C.; White, J. S.; Brongersma, M. L. *Nat. Mater.* **2010**, *9* (3), 193–204.

(3) Atwater, H. A.; Polman, A. *Nat. Mater.* **2010**, *9* (3), 205–13.

(4) Nie, S.; Emory, S. R. *Science* **1997**, *275* (5303), 1102–1106.

(5) Stipe, B. C.; Strand, T. C.; Poon, C. C.; Balamane, H.; Boone, T. D.; Katine, J. A.; Li, J.-L.; Rawat, V.; Nemoto, H.; Hirotsune, A.; Hellwig, O.; Ruiz, R.; Dobisz, E.; Kercher, D. S.; Robertson, N.; Albrecht, T. R.; Terris, B. D. *Nat. Photonics* **2010**, *4* (7), 484–488.

(6) Lal, S.; Link, S.; Halas, N. J. *Nat. Photonics* **2007**, *1* (11), 641–648.

(7) Pala, R. A.; White, J.; Barnard, E.; Liu, J.; Brongersma, M. L. *Adv. Mater.* **2009**, *21* (34), 3504–3509.

(8) Stockman, M. I.; Kling, M. F.; Kleineberg, U.; Krausz, F. *Nat. Photonics* **2007**, *1* (9), 539–544.

(9) Kim, S.; Jin, J.; Kim, Y.-J.; Park, I.-Y.; Kim, Y.; Kim, S.-W. *Nature* **2008**, *453* (7196), 757–760.

(10) Hao, F.; Larsson, E. M.; Ali, T. A.; Sutherland, D. S.; Nordlander, P. *Chem. Phys. Lett.* **2008**, *458* (4−6), 262–266.

(11) Liu, M.; Lee, T.-W.; Gray, S. K.; Guyot-Sionnest, P.; Pelton, M. *Phys. Rev. Lett.* **2009**, *102* (10), No. 107401.

(12) Yamamoto, N.; Araya, K.; García de Abajo, F. J. *Phys. Rev. B* **2001**, *64* (20), No. 205419.

(13) Giannini, V.; Fernández-Domínguez, A. I.; Sonnefraud, Y.; Roschuk, T.; Fernández-García, R.; Maier, S. A. *Small* **2010**, *6* (22), 2498–2507.

(14) Lewis, A.; Taha, H.; Strinkovski, A.; Manevitch, A.; Khatchatouriants, A.; Dekhter, R.; Ammann, E. *Nat. Biotechnol.* **2003**, *21* (11), 1378–1386.

(15) García de Abajo, F. J. *Rev. Mod. Phys.* **2010**, *82* (1), 209.

(16) Vogelgesang, R.; Dmitriev, A. *Analyst* **2010**, *135* (6), 1175–1181.

(17) Kuttge, M.; Vesseur, E. J. R.; Polman, A. *Appl. Phys. Lett.* **2009**, *94* (18), 183104−3.

(18) Gómez-Medina, R.; et al. *New J. Phys.* **2008**, *10* (10), No. 105009.

(19) Kuttge, M.; García de Abajo, F. J.; Polman, A. *Nano Lett.* **2010**, *10* (5), 1537–1541.

(20) Kociak, M.; Zagonel, L. F.; Mazzucco, S.; Tizei, L. H. G.; Stephan, O.; Tencé, M. *International Microscopy Conference XVII* **2010**, I1.10.

(21) García de Abajo, F. J.; Kociak, M. *Phys. Rev. Lett.* **2008**, *100* (10), No. 106804.

(22) Hohenester, U.; Ditlbacher, H.; Krenn, J. R. *Phys. Rev. Lett.* **2009**, *103* (10), No. 106801.

(23) Cord, B.; Lutkenhaus, J.; Berggren, K. K. *J. Vac. Sci. Technol., B* **2007**, *25* (6), 2013–2016.

(24) Yang, J. K. W.; Cord, B.; Duan, H.; Berggren, K. K.; Klingfus, J.; Nam, S.-W.; Kim, K.-B.; Rooks, M. J. *J. Vac. Sci. Technol., B* **2009**, *27*, 2622–2627.

(25) N'Gom, M.; Ringnalda, J.; Mansfield, J. F.; Agarwal, A.; Kotov, N.; Zaluzec, N. J.; Norris, T. B. *Nano Lett.* **2008**, *8* (10), 3200–3204.

(26) Nelayah, J.; Kociak, M.; Stephan, O.; de Abajo, F. J. G.; Tence, M.; Henrard, L.; Taverna, D.; Pastoriza-Santos, I.; Liz-Marzan, L. M.; Colliex, C. *Nat. Phys.* **2007**, *3* (5), 348–353.

(27) Chu, M.-W.; Myroshnychenko, V.; Chen, C. H.; Deng, J.-P.; Mou, C.-Y.; García de Abajo, F. J. *Nano Lett.* **2008**, *9* (1), 399–404.

(28) Koh, A. L.; Bao, K.; Khan, I.; Smith, W. E.; Kothleitner, G.; Nordlander, P.; Maier, S. A.; McComb, D. W. *ACS Nano* **2009**, *3* (10), 3015–3022.

(29) Song, F.; Wang, T.; Wang, X.; Xu, C.; He, L.; Wan, J.; Van Haesendonck, C.; Ringer, S. P.; Han, M.; Liu, Z.; Wang, G. *Small* **2010**, *6* (3), 446–451.

(30) Bosman, M.; et al. *Nanotechnology* **2007**, *18* (16), No. 165505.

(31) Boudarham, G.; Feth, N.; Myroshnychenko, V.; Linden, S.; García de Abajo, J.; Wegener, M.; Kociak, M. *Phys. Rev. Lett.* **2010**, *105* (25), No. 255501.

(32) Koh, A. L.; McComb, D. W.; Maier, S. A.; Low, H. Y.; Yang, J. K. W. *J. Vac. Sci. Technol., B* **2010**, *28*, C6045.

(33) Prodan, E.; Radloff, C.; Halas, N. J.; Nordlander, P. *Science* **2003**, *302* (5644), 419–422.

(34) Atay, T.; Song, J.-H.; Nurmikko, A. V. *Nano Lett.* **2004**, *4* (9), 1627–1631.

(35) Zuloaga, J.; Prodan, E.; Nordlander, P. *Nano Lett.* **2009**, *9* (2), 887–891.